Quantum spin Hall insulators with interactions and lattice anisotropy

Wei Wu,[1,2] Stephan Rachel,[1] Wu-Ming Liu,[2] and Karyn Le Hur[1]
[1]*Department of Physics, Yale University, New Haven, Connecticut 06520, USA*
[2]*Beijing National Laboratory for Condensed Matter Physics, Institute of Physics, Chinese Academy of Sciences, Beijing 100190, China*
(Received 15 June 2011; revised manuscript received 16 April 2012; published 2 May 2012)

We investigate the interplay between spin-orbit coupling and electron-electron interactions on the honeycomb lattice, combining the cellular dynamical mean-field theory and its real-space extension with analytical approaches. We provide a thorough analysis of the phase diagram and temperature effects at weak spin-orbit coupling. We systematically discuss the stability of the quantum spin Hall phase toward interactions and lattice anisotropy, resulting in the plaquette-honeycomb model. We also show the evolution of the helical edge states characteristic of quantum spin Hall insulators as a function of Hubbard interaction and anisotropy. At very weak spin-orbit coupling and intermediate electron-electron interactions, we substantiate the existence of a quantum spin liquid phase.

DOI: 10.1103/PhysRevB.85.205102 PACS number(s): 31.15.V−, 71.10.−w

I. INTRODUCTION

Time-reversal-invariant topological insulators[1]—bulk insulators with metallic surfaces—are characterized by a $\mathbb{Z}_2$ invariant[2,3] and cannot be adiabatically connected to trivial band-insulator phases unless the single-particle gap closes. While $\mathbb{Z}_2$ topological insulators (TIs) are robust against disorder,[4] rigorous and general results about the fate of TIs in the presence of prominent electron-electron interactions are limited.[5] Strongly correlated TIs as well as exotic time-reversal-invariant Mott-insulator phases have been predicted[6–12] apart from more conventional magnetically ordered phases.

By analogy to the quantum Hall effect, two-dimensional TIs are also named quantum spin Hall (QSH) insulators. It was originally proposed that they would be realized in graphene[2] and later also in HgTe/CdTe quantum wells,[13] where subsequent experiments[14] measuring a quantized conductance established the field of TIs. They possess an odd number of pairs of time-reversal-conjugate counterpropagating edge states (the helical edge states).[2,13–15] There are other promising proposals to stabilize the QSH effect in real materials: graphene endowed with heavy adatoms like indium and thallium[16] and synthesized silicene[17] were shown to exhibit a stable QSH phase. Particularly interesting are monolayers or thin films of iridium-based materials X_2IrO_3 (X = Na or Li) which have been suggested to possibly host QSH phases[18,19] since both spin-orbit coupling (SOC) and electron-electron interactions are quite strong in such materials. All these systems have in common the underlying honeycomb lattice, where recently a gapped quantum spin liquid for intermediate interactions was found using quantum Monte Carlo (QMC) simulations.[20–22]

Very recent progress in experiments on ultracold atoms in tunable optical lattices has established a second class of systems (besides iridium-based materials) where topological interacting phases might be realized. This progress is twofold: (i) tunable hexagonal lattices have been realized[23] and (ii) different types of spin-orbit interactions are feasible now.[24] Additional electron-electron on-site interactions are considered as a standard tool in optical lattices.[25] All these achievements in such a rapidly evolving field indicate that topological interacting phases within cold atoms will be demonstrated in the very near future.

In this paper, we investigate the interplay between SOC and electron-electron interactions on the honeycomb lattice and combine two paradigmatic models: to capture the nontrivial band topology we consider the Kane-Mele (KM) model[2] without the Rashba term and to describe interaction effects the Hubbard model, merging to the Kane-Mele-Hubbard (KMH) model.[8,21,22,26–28] Our goal is to combine the cellular dynamical mean-field theory[29–31] (CDMFT) and its real-space extension with analytical approaches, present our phase diagram at half filling including temperature effects, and thoroughly address the fate of helical edge states as a function of interactions and SOC. Additionally, we introduce the plaquette-honeycomb model which illustrates that the QSH phase is also stable toward lattice anisotropy.

II. THE KANE-MELE-HUBBARD MODEL

The KMH Hamiltonian on the honeycomb lattice reads

$$H = -t\sum_{\langle ij\rangle\sigma} c^{\dagger}_{i\sigma}c_{j\sigma} + i\lambda\sum_{\ll ij\gg\alpha\beta} \nu_{ij}c^{\dagger}_{i\alpha}\sigma^{z}_{\alpha\beta}c_{j\beta} + U\sum_{i} n_{i\uparrow}n_{i\downarrow}, \tag{1}$$

where i,j label the sites on the honeycomb lattice, $c_{i\sigma}$ is the electron annihilation operator, $n_{i\sigma} = c^{\dagger}_{i\sigma}c_{i\sigma}$, t is the hopping integral (t is our reference energy scale, and hence we set $t \equiv 1$), λ the SOC, U the on-site interaction, and $\nu_{ij} = \mathrm{sgn}[(\hat{\boldsymbol{d}}_i \times \hat{\boldsymbol{d}}_j)_z]$ where $\hat{\boldsymbol{d}}_{i/j}$ are the two vectors along the links from j to i ($\nu_{ij} = \pm 1$).[2] While the Hubbard model respects SU(2) spin and C_6 lattice symmetry, the SOC breaks the spin symmetry down to U(1) and the lattice to C_3 while it leaves time-reversal symmetry invariant. Details of the used CDMFT method and its real-space extension are provided in the Appendix.

For large interactions, the phase is an easy-plane antiferromagnet.[8] First, it is useful to start with a mean-field (MF) consideration of the TBI-SDW transition which can also be described within slave-rotor theory,[8] where the condensation of magnetic monopoles results in an XY instability. At $\lambda = 0$, Eq. (1) is spin rotationally invariant and a staggered magnetization pointing in any direction will be

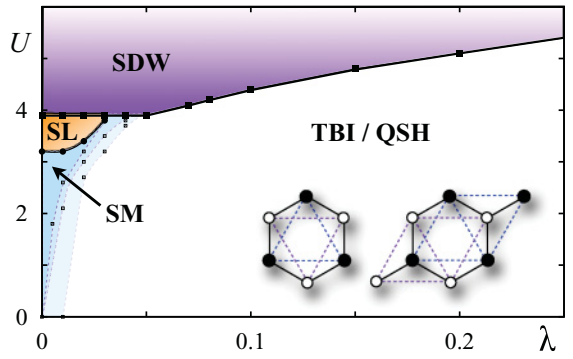

FIG. 1. (Color online) Phase diagram of the KMH model within CDMFT, including the four phases: (i) the topological band insulator (TBI), (ii) the magnetically ordered spin-density-wave (SDW) phase, (iii) the nonmagnetic insulator phase [spin liquid (SL)], and (iv) the semimetal (SM) region, shown (from right to left) for temperatures $T = 0.025$, 0.0125, and 0.005. Extrapolating to $T \to 0$, the SM region shrinks to a line; see the text. All other phase boundaries are extrapolated to $T = 0$. Inset: Typical clusters as used within the CDMFT.

a good order parameter. For finite λ, one can learn from the effective spin model[32] i.e., the strong-coupling limit of Eq. (1); cf. Ref. 8 that the magnetization lies in the XY plane. Hence we chose the order parameter accordingly, $m = \langle S_i^+ \rangle = \langle S_i^x \rangle + i\langle S_i^y \rangle$. From the Hubbard interaction we obtain $n_{i\uparrow}n_{i\downarrow} = -S_i^+ S_i^- + (n_{i\uparrow} + n_{i\downarrow})/2$. A standard MF decomposition results in $H_I \approx \sum_{\boldsymbol{k}} U[m(b_{\boldsymbol{k}\downarrow}^\dagger b_{\boldsymbol{k}\uparrow} - a_{\boldsymbol{k}\downarrow}^\dagger a_{\boldsymbol{k}\uparrow}) + m^\star(b_{\boldsymbol{k}\uparrow}^\dagger b_{\boldsymbol{k}\downarrow} - a_{\boldsymbol{k}\uparrow}^\dagger a_{\boldsymbol{k}\downarrow})] + \text{const}$, where the operators $a_{\boldsymbol{k}\sigma}$ and $b_{\boldsymbol{k}\sigma}$ are associated with the two sublattices. Eventually one obtains the MF spectrum $\varepsilon_\pm^{\text{MF}} = \pm\sqrt{|g(\boldsymbol{k})|^2 + \gamma(\boldsymbol{k})^2 + U^2|m|^2} + \text{const}$, and from there we find the MF equation. Note that $g(\boldsymbol{k})$ is the nearest-neighbor hopping and $\gamma(\boldsymbol{k})$ the second-neighbor (spin-orbit) Haldane term.[35] The transition line differs slightly from the analogous calculation with the order parameter $\langle S_i^z \rangle$. Mainly, the form of $\varepsilon_\pm^{\text{MF}}$ reveals that the mean-field approximation causes another mass term which does not compete with the SOC mass $\gamma(\boldsymbol{k})$. Consequently, when passing from the TBI to the SDW phase we do not expect closing of the single-particle gap. Indeed, within CDMFT no closing of the single-particle gap is observed (while the gap has a local minimum at the transition). We also computed $\langle S_i^x \rangle$ which becomes finite at the TBI-SDW transition (see also the Appendix); note that this transition is of three-dimensional (3D) XY universality at $T = 0$.

For very weak SOC we identify a small phase at intermediate U which is nonmagnetic, exhibits a finite spin gap, and is separated from the TBI phase by closing of the single-particle gap (see Fig. 3). This phase is reminiscent of the recently found quantum spin liquid (SL) phase;[20,21] in particular, the position and shape of this nonmagnetic insulator phase essentially coincide with the SL phase found within QMC calculations.[21] Here, we shall mention that since the CDMFT method approximates the self-energy by restricting it to the chosen cluster (see the inset of Fig. 1), the correlation length of this SL phase cannot be inferred. Note that at least a six-site cluster is required to observe the SL phase; see Fig. 2. We have plotted the single-particle gap Δ_{sp} and magnetization m for $\lambda = 0$ and various cluster sizes C. For $C = 2$ and 4 the single-particle gap and magnetization become finite simultaneously, while for $C \geqslant 6$ the onset of the two quantities

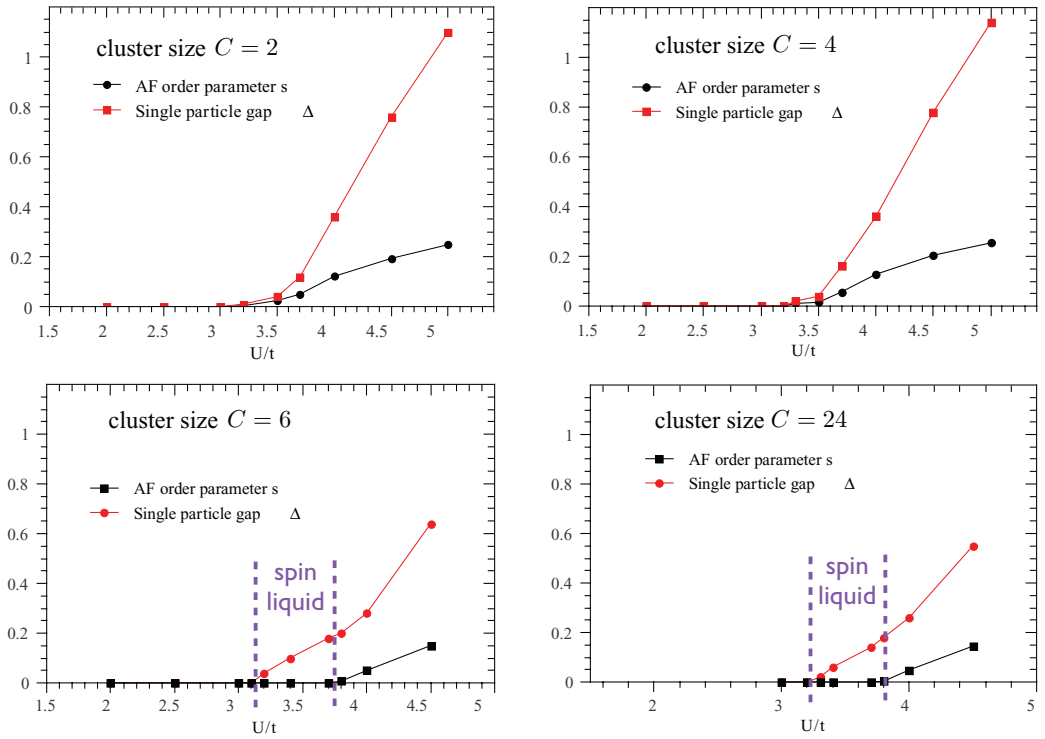

FIG. 2. (Color online) Single-particle gap Δ_{sp} and magnetization m as a function of U for $\lambda = 0$. The various panels correspond to different cluster sizes used by the CDMFT method. A minimal cluster size $C = 6$ is required to find the nonmagnetic insulator phase.

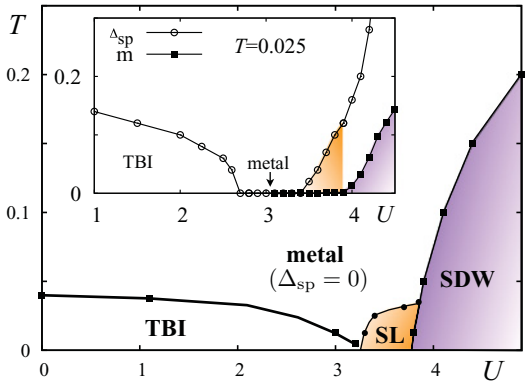

FIG. 3. (Color online) Temperature dependence of the phase diagram at SOC $\lambda = 0.02$. Inset: Single-particle gap Δ_{sp} and magnetization m vs U for $\lambda = 0.02$ and $T = 0.025$.

occurs for different U, indicating the SL phase. The existence of such possible spin-gapped phases on the honeycomb lattice has also been addressed theoretically.[36]

In the phase diagram of Fig. 1 there is an additional semimetal phase where the Dirac cones of graphene are preserved. Using QMC as the impurity solver, we systematically discuss temperature effects at weak SOC. We observe that the SL phase appears at very low temperatures (see Fig. 2) and that the SM domain prominently develops with temperature as the TBI gap is also very small when $\lambda \to 0$. For $T \to 0$, the SM phase reduces to a line pointing along the $\lambda = 0$ axis, which survives until relatively large interactions. From the renormalization group point of view, this SM line at $\lambda = 0$ is known to be stable for weak U.[37] Hence, we show the SM region for $T = 0.025$, 0.0125, and 0.005 in Fig. 1. Remember that both the SL and TBI phases at $\lambda \leqslant 0.03$ possess a small single-particle gap. In the inset of Fig. 3 we present the single-particle gap and magnetization for $\lambda = 0.02$ and $T = 0.025$. The evolution of the phase diagram with temperature is shown in Fig. 3 for $\lambda = 0.02$.

We use continuous-time quantum Monte Carlo (CTQMC) as an impurity solver which enables us to access finite temperatures. This is clearly an advantage of the method since experiments are performed at finite temperatures, but a careful interpretation of results is still needed. In Fig. 3, for instance, the SDW phase at finite T violating the Mermin-Wagner theorem is clearly an artifact of the CDMFT method. In contrast, the stability of the TBI phase with increasing temperature is reliable and important for experimentalists.

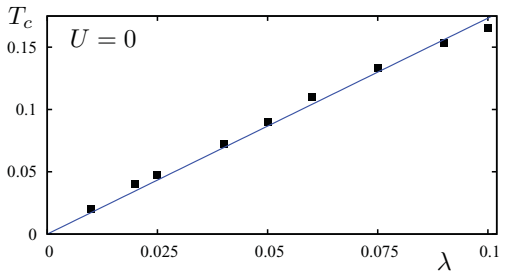

FIG. 4. (Color online) T_c as a function of λ for the TBI phase at $U = 0$. The blue line is a linear fit.

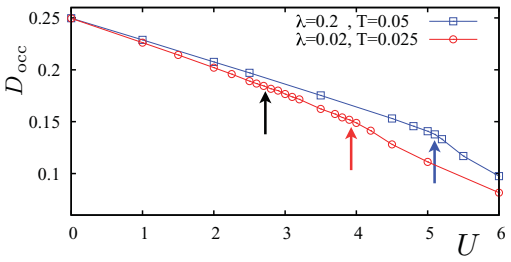

FIG. 5. (Color online) Double occupancy $\langle n_{i\uparrow} n_{i\downarrow} \rangle$ as a function of U for $\lambda = 0.02$ (red circles) and 0.2 (blue squares). The blue arrow (for $\lambda = 0.2$) at $U = 5.1$ and the red arrow (for $\lambda = 0.02$) at $U = 3.9$ mark the phase transition into the magnetically ordered phase. Note that the transition from the TBI (black arrow) to the SM phase cannot be resolved.

From an experimental perspective, it may be interesting to know how T_c can be raised and for what parameter settings T_c is conveniently large. Since the spin-orbit gap for $\lambda = 0.02$ is tiny, $T_c < 0.05$. An increase in λ (and the bulk gap), however, leads to an (approximately linear) increase of T_c up to $T_c > 0.16$ for $\lambda = 0.1$ and $U = 0$; see Fig. 4 where the line is a linear fit. We corroborate that the critical temperature T_c follows the gap at $T = 0$. For finite values of U a similar behavior of T_c is obtained. Note that T_c does not necessarily indicate a phase transition from TBI to metal; to clarify the precise nature of this boundary would require further work.

Within CDMFT, we also access the double occupancy $D_{\rm occ} = \langle n_{i\uparrow} n_{i\downarrow} \rangle = \partial F / \partial U$ where F is the free energy. In Fig. 5 we show that $D_{\rm occ}$, which measures the itinerant properties of electrons, is a useful quantity to detect the magnetically ordered phase.[31,38] The double occupancy is bounded as $1/4 \geqslant D_{\rm occ} \geqslant 0$. For $U = 0$, the ground state is a TBI with occupied lower and empty upper bands, $|\mathrm{TBI}\rangle = \prod_{\boldsymbol{k}} l^\dagger_{\boldsymbol{k}\uparrow} l^\dagger_{\boldsymbol{k}\downarrow} |0\rangle$, where $(a_{\boldsymbol{k}\sigma}, b_{\boldsymbol{k}\sigma})^T = T_\sigma (l_{\boldsymbol{k}\sigma}, u_{\boldsymbol{k}\sigma})^T$ and the matrices T_σ are given by

$$T_\uparrow = \begin{pmatrix} -\alpha_- & -\alpha_+ \\ \beta_- & \beta_+ \end{pmatrix}, \quad T_\downarrow = \begin{pmatrix} \alpha_+ & \alpha_- \\ \beta_+ & \beta_- \end{pmatrix} \tag{2}$$

with

$$\begin{aligned} \alpha_\pm &= \alpha_\pm(\boldsymbol{k}) = \mathcal{N}_\pm g(\boldsymbol{k})[\gamma(\boldsymbol{k}) \pm \varepsilon(\boldsymbol{k})]/|g(\boldsymbol{k})|^2, \\ \beta_\pm &= \beta_\pm(\boldsymbol{k}) = \mathcal{N}_\pm, \\ \mathcal{N}_\pm &= |g(\boldsymbol{k})|/\sqrt{|g(\boldsymbol{k})|^2 + [\gamma(\boldsymbol{k}) \pm \varepsilon(\boldsymbol{k})]^2}. \end{aligned} \tag{3}$$

Here $g(\boldsymbol{k})$ is the nearest-neighbor hopping term, $\gamma(\boldsymbol{k})$ is the Haldane term (second-neighbor spin-orbit hopping), and $\varepsilon(\boldsymbol{k}) = \sqrt{|g(\boldsymbol{k})|^2 + \gamma(\boldsymbol{k})^2}$ is the single-particle Kane-Mele energy spectrum. Essentially, the matrices T_σ contain the eigenvectors of the single-particle eigenstates. The Fermi level lies in the gap, $\varepsilon_F = 0$. Choosing a site i that belongs to the sublattice a we obtain

$$\begin{aligned} &\langle \mathrm{TBI}| n_{i\uparrow} n_{i\downarrow} |\mathrm{TBI}\rangle \\ &= \frac{1}{N^2} \sum_{\boldsymbol{k}_1 \boldsymbol{k}_2 \boldsymbol{k}_3 \boldsymbol{k}_4} e^{-i(\boldsymbol{k}_1 - \boldsymbol{k}_2 + \boldsymbol{k}_3 - \boldsymbol{k}_4)\boldsymbol{R}_i} \langle a^\dagger_{\boldsymbol{k}_1\uparrow} a_{\boldsymbol{k}_2\uparrow} a^\dagger_{\boldsymbol{k}_3\downarrow} a_{\boldsymbol{k}_4\downarrow} \rangle \\ &= \frac{1}{N^2} \sum_{\boldsymbol{k}_1 \boldsymbol{k}_2 \boldsymbol{k}_3 \boldsymbol{k}_4} e^{-i(\boldsymbol{k}_1 - \boldsymbol{k}_2 + \boldsymbol{k}_3 - \boldsymbol{k}_4)\boldsymbol{R}_i} \end{aligned}$$

$$\times\alpha_-^\star(\boldsymbol{k}_1)\alpha_-(\boldsymbol{k}_2)\alpha_+^\star(\boldsymbol{k}_3)\alpha_+(\boldsymbol{k}_4)\langle l^\dagger_{\boldsymbol{k}_1\uparrow}l_{\boldsymbol{k}_2\uparrow}l^\dagger_{\boldsymbol{k}_3\downarrow}l_{\boldsymbol{k}_4\downarrow}\rangle$$

$$= \frac{1}{N^2}\sum_{\boldsymbol{k}_1\boldsymbol{k}_3}|\alpha_-(\boldsymbol{k}_1)|^2|\alpha_+(\boldsymbol{k}_3)|^2, \quad (4)$$

where we used in the second last line $\langle l^\dagger_{\boldsymbol{k}_1\uparrow}l_{\boldsymbol{k}_2\uparrow}l^\dagger_{\boldsymbol{k}_3\downarrow}l_{\boldsymbol{k}_4\downarrow}\rangle = \delta_{\boldsymbol{k}_1\boldsymbol{k}_2}\delta_{\boldsymbol{k}_3\boldsymbol{k}_4}$ as well as $\langle u^\dagger_{\boldsymbol{k}\sigma}u_{\boldsymbol{k}\sigma}\rangle = 0$, $\langle u^\dagger_{\boldsymbol{k}\sigma}l_{\boldsymbol{k}\sigma}\rangle = 0$, and $\langle l^\dagger_{\boldsymbol{k}\sigma}l_{\boldsymbol{k}\sigma}\rangle = 1$. N refers to the number of unit cells. Using the relations

$$\sum_{\boldsymbol{k}}|\alpha_\pm(\boldsymbol{k})|^2 = \sum_{\boldsymbol{k}}|\beta_\pm(\boldsymbol{k})|^2 = N/2, \quad (5)$$

we confirm that

$$D_{\rm occ}|_{U=0} = \langle {\rm TBI}|{\rm n}_{\rm i\uparrow}{\rm n}_{\rm i\downarrow}|{\rm TBI}\rangle = \tfrac{1}{4}, \quad (6)$$

independent of λ in agreement with CDMFT; see Fig. 5. Above we considered without loss of generality $n_{i\sigma} = a^\dagger_{i\sigma}a_{i\sigma}$. Identical calculations performed with the $b_{i\sigma}$ operators which belong to the other sublattice yield, of course, the same result. In the opposite limit, $U\to\infty$, we clearly find $D_{\rm occ} = 0$ as a fingerprint of Mott physics since we impose half filling.

III. HELICAL EDGE STATES

To describe the edge states associated with QSH insulators, first we apply the concept of the helical Luttinger liquid (HLL).[15] Hence, we linearize the spectrum around the Fermi points and switch from lattice operators to field operators $\psi_{R\uparrow}(x)$ and $\psi_{L\downarrow}(x)$, which are right- and left-moving fields, respectively; we obtain for the noninteracting part $H_0 = v_F\int dx(\psi^\dagger_{R\uparrow}i\partial_x\psi_{R\uparrow} - \psi^\dagger_{L\downarrow}i\partial_x\psi_{L\downarrow})$. Note that a standard single-particle (disorder) backscattering term $\psi^\dagger_{R\uparrow}\psi_{L\downarrow} + {\rm H.c.}$, which opens up a mass gap in the spinless Luttinger liquid, is not allowed since the model is odd under time-reversal symmetry, $\mathcal{T}^2 = -1$. Only two time-reversal-invariant interactions are allowed: the forward scattering as well as the umklapp scattering $\sim\psi^\dagger_{R\uparrow}\psi^\dagger_{R\uparrow}\psi_{L\downarrow}\psi_{L\downarrow}$ which is not intrinsically present in the Hubbard model. Instead we shall include the forward interaction $H_I = U\int dx(\psi^\dagger_{R\uparrow}\psi_{R\uparrow}\psi^\dagger_{L\downarrow}\psi_{L\downarrow})$. As long as there is no magnetic order in the bulk, $(H_0 + H_I)$ can be solved exactly by resorting to bosonization which results in power-law decaying spin and charge correlations in the HLL. This result is also obtained through a spin-wave analysis at the edges for weak interactions.[39] It is worth mentioning that, in contrast, spin-spin correlation functions in the bulk decay very rapidly.[8]

At the SDW transition, H_I turns into $H_I \approx -Um\int dx\,\psi^\dagger_{L\downarrow}\psi_{R\uparrow} + {\rm H.c.}$ with $m = \langle\psi^\dagger_{R\uparrow}\psi_{L\downarrow}\rangle$; applying the bosonization procedure and introducing the Luttinger parameter K as usual, the Hamiltonian becomes

$$H = \int dx\frac{v}{2}\left[\frac{1}{K}(\partial_x\phi)^2 + K(\partial_x\theta)^2\right] - \frac{Um\sin\sqrt{4\pi}\phi}{(\pi a)^2}. \quad (7)$$

Here, v is the renormalized plasmon velocity and a the lattice spacing, the field ϕ contains both spin and charge degrees of freedom, and $\partial_x\theta$ and ϕ are conjugate variables.[15] The sine-Gordon term is a relevant perturbation for repulsive interactions (since $K \ll 2$) and hence, through the pinning of the ϕ field, the edge modes acquire a charge gap at the SDW transition. We can also check that the spin sector at the edges is described by an Ising order characterized by $\langle S^x_i\rangle \neq 0$ and $\langle S^y_i\rangle = 0$. This shows that the SDW transition affects the charge sector of the HLL in a nontrivial way, resulting in a metal-insulator transition of Kosterlitz-Thouless type. Note that the disordering-ordering transition in the spin sector also influences the charge properties of the edges.

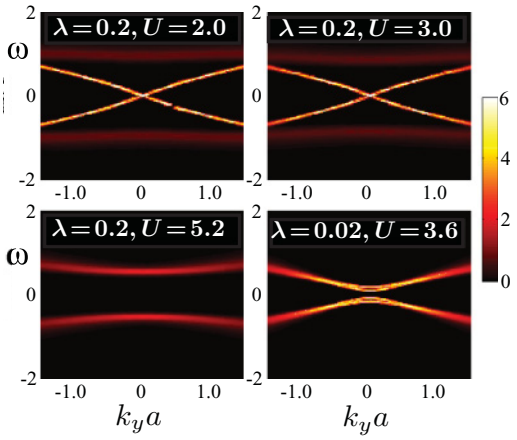

FIG. 6. (Color online) Spectral function $A(k_y,\omega)$ for a cylinder geometry with armchair edges ($L = 96$, $T = 0.05$). Top: helical edge states of the QSH phase with $\lambda = 0.2$ and $U = 2.0$ or 3.0, respectively. Bottom, left: for $U = 5.2 > U_c$ (SDW phase) the helical edge states disappear while the single-particle gap remains finite. Bottom, right: $A(k_y,\omega)$ inside the SL phase; no edge states cross the gap. The color bar corresponds to the intensity of $A(k_y,\omega)$.

In addition, we performed CDMFT simulations on honeycomb cylinders with length $x = (3a/4)L$ with both armchair and zigzag edges (L is the number of sites in the x direction). By computing the spectral function $A(k_y,\omega)$ we extract the edge state spectrum in the presence of interactions. In contrast to previous work[21] we treat the full microscopic Hamiltonian. We observe the following: (i) The plasmon velocity v associated with the edge modes slightly decreases for increasing U as expected from the HLL. (ii) The intensity of the spectral function decreases with increasing U. (iii) The edge modes gap out when $\langle S^x_i\rangle$ becomes finite. In Fig. 6 we show exemplarily the edge modes for fixed $\lambda = 0.2$, armchair boundary conditions, and $U = 2.0$, 3.0, and 5.2.

We further performed computations for the spectral function on zigzag ribbons. Now, in contrast to the armchair case, the periodic boundary conditions are imposed in the x direction, yielding k_x as a good quantum number. For zigzag edges one extracts the more familiar spectrum[2] of the KM model at small λ (see Fig. 7, top): the edge states connect the upper band of a gapped Dirac cone $\boldsymbol{K}$ with the lower band of the other gapped Dirac cone $\boldsymbol{K}'$, and vice versa. In addition, we have also shown the situation for stronger SOC $\lambda = 0.2$ (see Fig. 7, bottom) where the bulk spectrum is relatively flat. Both spectral functions are computed for $U = 2.0$. The main findings (i)–(iii) obtained for armchair ribbons also apply for zigzag ribbons.

We also computed the spectral function on a cylinder for parameters U and λ which belong to the spin liquid phase (see Fig. 6). Although the single-particle gap is very small we did not find edge states inside the gap. While it is not known

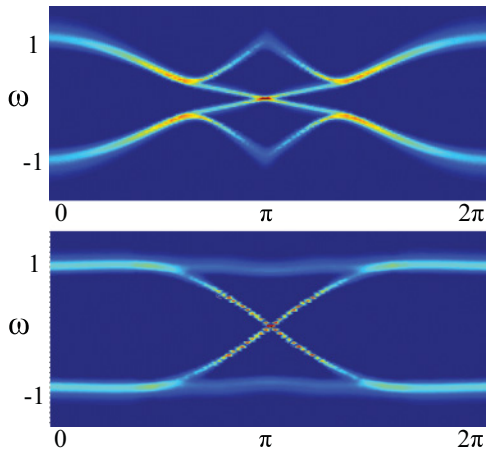

FIG. 7. (Color online) Spectral functions for a zigzag ribbon at $\lambda = 0.05$ and $U = 2.0$ (top) and at $\lambda = 0.2$ and $U = 2.0$ (bottom).

whether the *true* SL exhibits edge states, the nonmagnetic insulator phase found within CDMFT is topologically trivial and absence of edge states is expected.

IV. PLAQUETTE-HONEYCOMB MODEL

Next, we show that the QSH phase is stable not only toward relatively large interactions but also to lattice anisotropy, resulting in the plaquette-honeycomb model, as sketched in the inset of Fig. 8. Hopping amplitudes which connect yellow plaquettes are $t' = \alpha t$ while hopping amplitudes inside a cluster are t. Spin-orbit couplings λ and $\lambda' = \alpha\lambda$ are analogously defined. In the absence of spin-orbit couplings, note that this type of anisotropy immediately opens a gap at the Dirac points. Mostly, when $\alpha \to 0$, we check that the spectrum exhibits flat bands associated with localized states on a given hexagon, hence resulting in the plaquette insulator (PI) in Fig. 8. Also, for large α, the system is an insulator (I) at the Fermi level. For finite SOC λ, we find that the QSH phase is stable over a large region of the phase diagram (containing the KM model at $\alpha = 1$). The gap closes at the phase transition between the PI/I and the QSH phase, yielding a SM phase boundary.

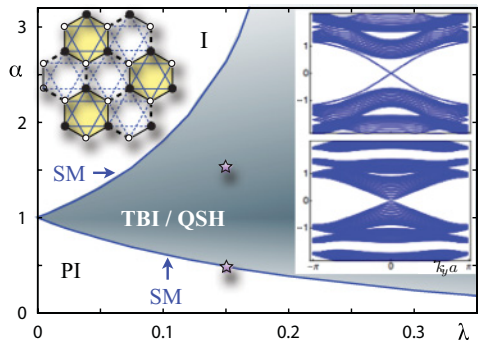

FIG. 8. (Color online) Zero-temperature α-λ phase diagram of the plaquette-honeycomb model at $U = 0$. The $\alpha = 1$ line corresponds to the KM model. Spectra for armchair ribbons ($L = 96$) are shown at $\lambda = 0.15, \alpha = 1.5$ (top, QSH phase) and $\alpha = 0.48$ (bottom, entrance of PI phase). Blue lines correspond to SM.

These SM lines are stable in the presence of finite electron-electron interactions U up to a critical $U_c(\alpha,\lambda)$ which is of comparable size to $U_c(1,\lambda)$ (i.e., for the isotropic KMH model). Preliminary results for some parameters indicate that for $U > U_c(\alpha \neq 1,\lambda)$ there is a nonmagnetic insulator phase as in the $\alpha = 1$ case. A detailed investigation of the interacting phase diagram of this plaquette-honeycomb model is left for future studies.

V. CONCLUSION

To summarize, through a combination of CDMFT and complementary approaches, we have substantiated that the QSH phase is robust toward prominent electron-electron interactions and lattice anisotropies. We have provided a quantitative analysis of the edge state properties which shows that the ordering transition for the spins is also accompanied by a metal-insulator transition at the edges. For very weak SOC, we have also confirmed the existence of a spin-gapped insulating phase. Finally, we have introduced an anisotropic version of the KM model with the potential to host a rich phase diagram when the Hubbard interaction is included.

ACKNOWLEDGMENTS

We acknowledge discussions with F. F. Assaad, G. Fiete, M. Hohenadler, T. Lang, and G. C. Liu. This work was supported by NSF Grant No. DMR-0803200 (K.L.H. and S.R.) and by NSFC under Grants No. 10874235, No. 10934010, and No. 60978019, by NKBRSFC under Grants No. 2009CB930701, No. 2010CB922904, and No. 2011CB921500 (W.W. and W.M.L.). We acknowledge the Yale High Performance Computing Center and the supercomputing center of CAS for kindly allocating computational resources.

APPENDIX: CDMFT METHOD

In order to investigate edge states within CDMFT we use the real-space extension of the homogeneous CDMFT method.[29,30] We consider (nano)ribbons (i.e., cylinder geometry) with translation symmetry in the direction along the edges (which we aligned for armchair ribbons along the y axis).

Within CDMFT we map the original honeycomb lattice onto an N_c-site effective cluster embedded in a self-consistent medium. The effective cluster model is obtained via an iterative procedure which can be started with an initial guess for the cluster self-energy $\Sigma(i\omega)$. The effective medium represented by the dynamical mean field, which is also known as the Weiss function $g_c(i\omega)$, is determined by the cluster self-energy $\Sigma(i\omega)$ via the coarse-grained Dyson equation.[31] Since the translation symmetry in the x direction is broken, we shall use the real-space CDMFT coarse-grained Dyson equation for the inhomogeneous system:

$$g_c^{-1}(i\omega) = \left[\sum_{k_y} \frac{1}{i\omega + \mu - t(k_y) - \Sigma(i\omega)}\delta_{I,J}\right]^{-1} + \Sigma(i\omega). \tag{A1}$$

Both g_c and Σ are block-diagonal matrices with block size N_c and dimension $[(N_c \times N_x) \times (N_c \times N_x)]$. I, J are block

indices, N_c is the cluster size, and N_x is the number of clusters after performing the dimensional reduction, i.e., N_x corresponds to the *height* of the ribbon.

Once $g_c(i\omega)$ is determined, the impurity solver[40] can be used to compute the effective many-body impurity problem to obtain the full Green's function G_c. Eventually, by using the Dyson equation of the cluster system $\Sigma(i\omega) = g_c^{-1}(i\omega) - G_c^{-1}(i\omega)$, we recalculate the self-energy $\Sigma(i\omega)$ to finish the iterative loop. The CDMFT self-consistent iterative loop should be repeatedly carried out, until numerical convergence has been reached.

Note that we use the spinor notation $\Psi^\dagger = \{c^\dagger_{i\uparrow}, c^\dagger_{i\downarrow}\}$ ($i \in$ cluster) and $\Psi = (\Psi^\dagger)^\dagger$ since a spontaneous transverse magnetization mixes the $\uparrow$ and $\downarrow$ spin parts of the system. Therefore the Green's function in the CDMFT framework takes the following form:

$$\langle \Psi(\tau_i)\Psi^\dagger(\tau_j)\rangle = \begin{bmatrix} G_{\uparrow\uparrow}(\tau_i-\tau_j) & G_{\uparrow\downarrow}(\tau_i-\tau_j) \\ G_{\downarrow\uparrow}(\tau_i-\tau_j) & G_{\downarrow\downarrow}(\tau_i-\tau_j) \end{bmatrix}. \quad \text{(A2)}$$

From the above procedure we can easily obtain the quantites $D_{\rm occ}$ (Refs. 31,38) and $\langle S^x\rangle$. The double occupancy $D_{\rm occ} = \langle n_{i\uparrow}n_{i\downarrow}\rangle = \partial F/\partial U$, as the first derivative of the free energy, is an important quantity in studies of strongly correlated systems. As $D_{\rm occ}$ is directly related to the potential energy, this is an indicator of the transition order. In the following, we suppress the site index i of the electron operators. Using the notation of Eq. (A2) we find

$$\begin{aligned} D_{\rm occ} &= \langle c^\dagger_\uparrow c_\uparrow c^\dagger_\downarrow c_\downarrow\rangle = \langle T_\tau c^\dagger_\uparrow(\tau_3)c_\uparrow(\tau_2)c^\dagger_\downarrow(\tau_1)c_\downarrow(0)\rangle \\ &= \langle T_\tau c^\dagger_\uparrow(\tau_3)c_\uparrow(\tau_2)\rangle\langle T_\tau c^\dagger_\downarrow(\tau_1)c_\downarrow(0)\rangle \\ &\quad - \langle T_\tau c^\dagger_\uparrow(\tau_3)c_\downarrow(0)\rangle\langle T_\tau c^\dagger_\downarrow(\tau_1)c_\uparrow(\tau_2)\rangle \\ &= G_{\uparrow\uparrow}(0^-)G_{\downarrow\downarrow}(0^-) - G_{\downarrow\uparrow}(0^-)G_{\uparrow\downarrow}(0^+), \end{aligned} \quad \text{(A3)}$$

where $0 < \tau_1 < \tau_2 < \tau_3$, and we used Wick's theorem.

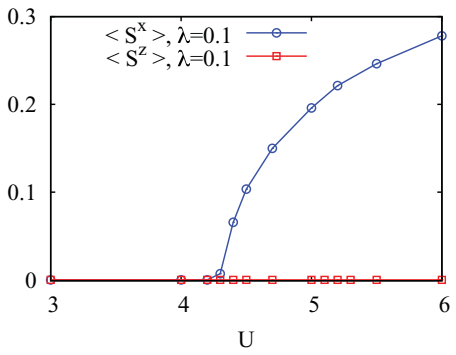

FIG. 9. (Color online) $\langle S^x\rangle$ and $\langle S^z\rangle$ versus U for $\lambda = 0.1$.

The transverse magnetic order parameter $\langle S^x_i\rangle$ reads $\langle S^x_i\rangle = \frac{1}{2}\langle c^\dagger_{i\uparrow}c_{i\downarrow} + \text{H.c.}\rangle$ which can be expressed through the Green's functions defined above,

$$\langle S^x_i(\tau = 0^-)\rangle = \tfrac{1}{2}\{G_{\uparrow\downarrow}(0^-) + G_{\downarrow\uparrow}(0^-)\}. \quad \text{(A4)}$$

In Fig. 9 we show both $\langle S^x\rangle = \langle S^x_i\rangle$ and $\langle S^z\rangle = \langle S^z_i\rangle$ vs U for $\lambda = 0.1$. Since the SOC breaks the spin-rotational invariance the magnetization is inside the XY plane; consequently we find a finite value of $\langle S^x\rangle$ at the transition into the SDW phase while $\langle S^z\rangle$ remains zero.

In the case of armchair ribbons and calculations with periodic boundary conditions (PBC) we used a six-site cluster and for zigzag ribbons an eight-site cluster; see inset of Fig. 1. In addition, we performed some PBC calculations with the eight-site cluster as well as with a 24-site cluster (see inset of Fig. 8). We found good quantitative agreement between the results performed with the different clusters, which underlines the reliability of the CDMFT method. But we would like to emphasize that a six-site cluster is needed to observe the spin liquid phase. For smaller cluster sizes (2 and 4) the spin liquid phase cannot be found, as shown in Fig. 2.

[1] M. Z. Hasan and C. L. Kane, Rev. Mod. Phys. **82**, 3045 (2010); J. Moore, Nature (London) **464**, 194 (2010); X.-L. Qi and S.-C. Zhang, Rev. Mod. Phys. **83**, 1057 (2011).
[2] C. L. Kane and E. J. Mele, Phys. Rev. Lett. **95**, 146802 (2005); **95**, 226801 (2005).
[3] J. E. Moore and L. Balents, Phys. Rev. B **75**, 121306(R) (2007).
[4] A. P. Schnyder, S. Ryu, A. Furusaki, and A. W. W. Ludwig, Phys. Rev. B **78**, 195125 (2008); E. Prodan, T. L. Hughes, and B. A. Bernevig, Phys. Rev. Lett. **105**, 115501 (2010).
[5] C. Xu and J. E. Moore, Phys. Rev. B **73**, 045322 (2006); M. Levin and A. Stern, Phys. Rev. Lett. **103**, 196803 (2009); Z. Wang, X.-L. Qi and S.-C. Zhang, *ibid.* **105**, 256803 (2010); V. Gurarie, Phys. Rev. B **83**, 085426 (2011).
[6] D. A. Pesin and L. Balents, Nat. Phys. **6**, 376 (2010).
[7] M. W. Young, S.-S. Lee, and C. Kallin, Phys. Rev. B **78**, 125316 (2008).
[8] S. Rachel and K. Le Hur, Phys. Rev. B **82**, 075106 (2010).
[9] J. Goryo *et al.*, J. Phys. Soc. Jpn. **80**, 044707 (2011).
[10] S. Raghu, X.-L. Qi, C. Honerkamp, and S.-C. Zhang, Phys. Rev. Lett. **100**, 156401 (2008).
[11] W. Witczak-Krempa, T. P. Choy, and Y. B. Kim, Phys. Rev. B **82**, 165122 (2010).
[12] M. Kargarian, J. Wen, and G. A. Fiete, Phys. Rev. B **83**, 165112 (2011).
[13] B. A. Bernevig, T. L. Hughes, and S.-C. Zhang, Science **314**, 1757 (2006).
[14] M. König *et al.*, Science **318**, 766 (2007).
[15] C. Wu, B. A. Bernevig, and S.-C. Zhang, Phys. Rev. Lett. **96**, 106401 (2006).
[16] C. Weeks *et al.*, Phys. Rev. X **1**, 021001 (2011).
[17] C.-C. Liu, W. Feng, and Y. Yao, Phys. Rev. Lett. **107**, 076802 (2011).
[18] A. Shitade, H. Katsura, J. Kunes, X. L. Qi, S. C. Zhang, and N. Nagaosa, Phys. Rev. Lett. **102**, 256403 (2009).
[19] Y. Singh and P. Gegenwart, Phys. Rev. B **82**, 064412 (2010).
[20] Z. Y. Meng *et al.*, Nature (London) **464**, 847 (2010).

[21]M. Hohenadler, T. C. Lang, and F. F. Assaad, Phys. Rev. Lett. **106**, 100403 (2011).
[22]D. Zheng, C. Wu, and Z. Zhong, Phys. Rev. B **84**, 205121 (2011).
[23]P. Soltan-Panahi *et al*., Nat. Phys. **7**, 434 (2011).
[24]Y.-J. Lin *et al*., Nature (London) **462**, 628 (2009); N. Goldman, I. Satija, P. Nikolic, A. Bermudez, M. A. Martin-Delgado, M. Lewenstein, and I. B. Spielman, Phys. Rev. Lett. **105**, 255302 (2010); J. Dalibard *et al*., Rev. Mod. Phys. **83**, 1523 (2011); Y.-J. Lin *et al*., Nature (London) **471**, 83 (2011).
[25]I. Bloch, J. Dalibard, and W. Zwerger, Rev. Mod. Phys. **80**, 885 (2008).
[26]D. Soriano and J. Fernandez-Rossier, Phys. Rev. B **82**, 161302(R) (2010); D. Gosalbez-Martinez, D. Soriano, J. J. Palacios, and J. Fernandez-Rossier, e-print arXiv:1203.2479.
[27]Y. Yamaji and M. Imada, Phys. Rev. B **83**, 205122 (2011).
[28]S.-L. Yu, X. C. Xie, and J.-X. Li, Phys. Rev. Lett. **107**, 010401 (2011).
[29]G. Kotliar *et al*., Rev. Mod. Phys. **78**, 865 (2006).
[30]T. Maier *et al*., Rev. Mod. Phys. **77**, 1027 (2005).
[31]W. Wu, Y. H. Chen, H. S. Tao, N. H. Tong, and W. M. Liu, Phys. Rev. B **82**, 245102 (2010).
[32]The effective spin Hamiltonian of the KMH model introduced in Ref. 8 is an anisotropic version of the J_1-J_2 model which was recently studied in Refs. 33 and 34.
[33]J. Reuther, D. A. Abanin, and R. Thomale, Phys. Rev. B **84**, 014417 (2011).
[34]A. F. Albuquerque, D. Schwandt, B. Hetenyi, S. Capponi, M. Mambrini, and A. M. Läuchli, Phys. Rev. B **84**, 024406 (2011).
[35]F. D. M. Haldane, Phys. Rev. Lett. **61**, 2015 (1988).
[36]C. Xu and S. Sachdev, Phys. Rev. Lett. **105**, 057201 (2010); Y.-M. Lu and Y. Ran, Phys. Rev. B **84**, 024420 (2011).
[37]V. N. Kotov *et al*., e-print arXiv:1012.3484, Rev. Mod. Phys. (to be published).
[38]E. V. Gorelik, I. Titvinidze, W. Hofstetter, M. Snoek, and N. Blumer, Phys. Rev. Lett. **105**, 065301 (2010).
[39]D.-H. Lee, Phys. Rev. Lett. **107**, 166806 (2011).
[40]A. N. Rubtsov, V. V. Savkin, and A. I. Lichtenstein, Phys. Rev. B **72**, 035122 (2005).